Journal of Materials Chemistry A

PAPER

View Article Online
View Journal | View Issue

Check for updates

Cite this: J. Mater. Chem. A, 2019, 7, 13284

B-terminated (111) polar surfaces of BP and BAs: promising metal-free electrocatalysts with large reaction regions for nitrogen fixation†

Zhe Chen,[ab] Jingxiang Zhao,*[a] Lichang Yin*[b] and Zhongfang Chen*[c]

The nitrogen electroreduction reaction (NRR) in aqueous solutions under ambient conditions represents an attractive prospect to produce ammonia, but the development of long-term stable and low-cost catalysts with high-efficiency and high-selectivity remains a great challenge. Herein, we investigated the potential of a new class of experimentally available boron-containing materials, *i.e.*, cubic boron phosphide (BP) and boron arsenide (BAs), as metal-free NRR electrocatalysts by means of density functional theory (DFT) calculations. Our results revealed that gas phase N_2 can be sufficiently activated on the B-terminated (111) polar surfaces of BP and BAs, and effectively reduced to NH_3 *via* an enzymatic pathway with an extremely low limiting potential (−0.12 V on BP and −0.31 V on BAs, respectively). In particular, the two proposed B-terminated (111) surfaces not only have a large active region for N_2 reduction, but also can significantly inhibit the competitive hydrogen evolution reaction, and thus have rather high efficiency and selectivity for the NRR. Therefore, cubic BP or BAs with mainly exposed (111) facets may serve as promising metal-free NRR catalysts with superior performance.

Received 5th February 2019
Accepted 12th April 2019

DOI: 10.1039/c9ta01410a

rsc.li/materials-a

1. Introduction

Ammonia, one of the most important synthetic chemicals for human sustainable development, is not only a carbon-free energy carrier but also of great significance for fertilizer production.[1–4] In industry, NH_3 has been routinely produced by the Haber–Bosch process for more than 100 years, in which gaseous N_2 and H_2 molecules are first dissociated into atomic N and H species, followed by their bonding to form NH_3 on conventional Fe- or Ru-based catalysts. In this process, however, high temperature (about 300–500 °C) and high pressure (about 150–300 atm) are required to directly split the inert and strong N≡N bond.[5–7] In addition, this conventional NH_3 synthesis process consumes more than 1% of the global energy, and is accompanied by huge greenhouse gas emission.[8,9] Thus, it is highly desirable to develop alternative strategies for NH_3 synthesis.[10,11]

The electrochemical nitrogen reduction reaction (NRR) under ambient conditions is very attractive due to its much reduced energy input and favorable environmental compatibility,[12,13] in which electrocatalysts are the core components to reduce the reaction overpotential and increase the reaction rate and selectivity of N_2 reduction.[14,15] Currently, transition metal-based NRR electrocatalysts working under ambient conditions have been widely investigated both experimentally and theoretically, including metal nitrides and oxides or single metal atoms anchored on various substrates.[16–23] However, the practical application of these metal-based NRR electrocatalysts has been severely limited by their low selectivity, high overpotential, easy deactivation, and detrimental environmental impact.[9,13,24]

In recent years, emerging metal-free catalysts for the NRR have attracted increasing attention due to their intrinsic advantages, such as low cost, high reliability, good biocompatibility, and excellent sustainability. In particular, boron-based heterogeneous electrocatalysts have been demonstrated their strong potential to capture and convert N_2 molecules to NH_3 in aqueous solutions under ambient conditions based on the so-called "acceptance–donation" mechanism.[25,26] For example, Yu *et al.* experimentally confirmed that boron-doped graphene with a doping level of 6.2% could achieve a NH_3 production rate of 9.8 μg hr^{-1} cm^{-2} and a Faradaic efficiency of 10.8% at −0.5 V *versus* the reversible hydrogen electrode.[27] Ling *et al.* proposed that a B atom anchored on graphitic-carbon nitride (g-C_3N_4) could be utilized as a metal-free NRR photocatalyst under visible light irradiation with a record low onset potential (−0.20 V).[28] Qiu *et al.* revealed that boron carbide (B_4C) nanosheets could act as a metal-free catalyst for high-performance electrochemical nitrogen-to-ammonia fixation, and

[a]College of Chemistry and Chemical Engineering, Key Laboratory of Photonic and Electronic Bandgap Materials, Ministry of Education, Harbin Normal University, Harbin, 150025, China. E-mail: xjz_hmily@163.com

[b]Shenyang National Laboratory for Materials Science, Institute of Metal Research, Chinese Academy of Sciences, Shenyang, 110016, China. E-mail: lcyin@imr.ac.cn

[c]Department of Chemistry, University of Puerto Rico, Rio Piedras Campus, San Juan, PR, 00931, USA. E-mail: zhongfangchen@gmail.com

† Electronic supplementary information (ESI) available. See DOI: 10.1039/c9ta01410a

could achieve a high ammonia yield of 26.57 μg h^{-1} mg^{-1} and a fairly high Faradaic efficiency of 15.95% at −0.75 V *versus* the reversible hydrogen electrode.[29] Though significant progress has been made, it is still a big challenge to develop highly efficient electrocatalysts with large reaction regions (or high concentration of B species), to fully achieve their catalytic activity.

From this perspective, we intuitively speculate that the most common B-containing compounds in III–V semiconductors, such as cubic boron nitride (BN), boron phosphide (BP) and boron arsenide (BAs), may show possible NRR activity. Note that these cubic III–V semiconductors are experimentally available, and their applications as high thermal conductivity materials have attracted great attention. Moreover, cubic BP is a promising electronic material for application in harsh environments, due to its good stability at high temperatures, high mechanical hardness, modest band gap (2.00 eV), and a high dielectric constant.[30,31] Recently synthesized high-purity cubic BAs[32] has similar electronic properties to Si[33] with a moderate band gap (1.50 eV),[34] and thus it is promising for applications in electronics and photovoltaics. However, cubic BN is not suitable for electroreduction application because of its extremely large band gap of around 6 eV.[35]

Considering the high abundance of B species in cubic BP and BAs, an interesting question arises: can the experimentally available cubic BP and BAs be directly utilized as metal-free electrocatalysts for the NRR? To address this question in this work, by means of comprehensive density functional theory (DFT) computations, we explored the catalytic performance of their (100), (110), and (111) surfaces towards the NRR. Our computations showed that among these three considered surfaces, the B-terminated (111) surface exhibits the highest NRR catalytic activity with a low limiting potential (−0.12 V for BP and −0.31 V for BAs, respectively) *via* an enzymatic reduction mechanism. Meanwhile, the hydrogen evolution side reaction can be significantly inhibited, suggesting high selectivity towards the NRR. Therefore, B-terminated (111) surfaces of cubic BP and BAs are quite promising metal-free electrocatalysts for the NRR with a large active region and high efficiency and selectivity, which opens a new door for the advancement of sustainable NH_3 production.

2. Computational methods

Spin-polarized DFT computations were performed using the Vienna *Ab Initio* Simulation Package (VASP) unless stated otherwise.[36] The exchange-correlation energy was represented by the Perdew–Burke–Ernzerhof (PBE) functional within the generalized gradient approximation (GGA) and the electron–ion interactions were described by the projector augmented wave (PAW) method.[37–39] The (100), (110), and (111) surfaces of cubic BP and BAs were constructed to explore the possible NRR activity. All these surfaces consist of four BP/BAs atomic layers, which are thick enough for energy convergence based on the test calculations (Table S1†). The bottom two BP/BAs atomic layers were fixed, while atoms in the other layers were fully relaxed during geometry optimizations. A 4 × 4 supercell was used for the (100) and (111) surfaces, while a 3 × 4 supercell was employed for the (110) surface in order to obtain a similar supercell size. Dipole correction was employed to correct potential spurious terms arising from the asymmetry of the slabs.[40] A Monkhorst–Pack *k*-point mesh of 3 × 3 × 1 was used to sample the Brillouin zone, and the plane-wave cut-off energy was set to be 500 eV. All the structures were fully relaxed until the force on each atom (except for the fixed ones) was less than 0.03 eV $Å^{-1}$ and the convergence criterion for the electronic structure iteration was set to be 10^{-5} eV. The van der Waals (vdW) interactions were described by using the empirical correction in Grimme's method (DFT+D3).[41] The vacuum space was set to be 20 Å in the *z* direction, which was large enough to minimize the interactions between periodic images. The climbing image nudged elastic band (CI-NEB) method was used to find saddle points and minimum-energy paths.[42] Hirshfeld population analysis[43] was performed using the PBE functional with a DNP basis set using the DMol^3 program.[44]

To investigate the thermodynamic stability of different surfaces under examination, we firstly calculated the surface energy (γ_s) following the definition $\gamma_s = \frac{1}{2A}(E^{relax}_{surface} - N_{atoms} \times E_{bulk})$, where A is the surface area, $E^{relax}_{surface}$ is the energy of the relaxed surface, N_{atoms} is the number of atoms in the slab, and E_{bulk} is the bulk energy per atom. According to this definition, the surface with a smaller γ_s value has a higher thermodynamic stability and higher probability of natural exposure. To further evaluate the thermal stability of relevant surfaces, *ab initio* molecular dynamics (AIMD) simulations were performed in the canonical ensemble (NVT) with a Nose–Hoover thermostat at 500 K for a time period of 10 ps with a time step of 2 fs.[45,46]

The adsorption energies (E_{ads}) of the NRR intermediates were determined by $E_{ads} = E_{total} - E_{slab} - E_{adsorbate}$, where E_{total}, E_{slab} and $E_{adsorbate}$ represent the total energies of the species-adsorbed slab system, the clean slab, and the adsorbate, respectively. According to this definition, a more negative adsorption energy indicates a stronger adsorption.

The Gibbs reaction free energy change (ΔG) of each elementary step in the NRR process was calculated by using the computational hydrogen electrode (CHE) model proposed by Nørskov *et al.*,[47] in which the chemical potential of the proton–electron pair in aqueous solution is equal to one-half of the chemical potential of a hydrogen molecule. Based on this model, the ΔG value can be obtained using $\Delta G = \Delta E + \Delta ZPE - T\Delta S + \Delta G_{pH} + eU$, where ΔE is the reaction energy of the reactant and product species adsorbed on the catalyst surface directly obtained from DFT computations and ΔZPE and ΔS are the changes of zero point energies and entropies between the adsorbed species and the gas phase molecules at 298.15 K, which were calculated from the vibrational frequencies. ΔG_{pH} is the free energy correction of pH, which can be calculated using $\Delta G_{pH} = K_B T \times pH \times \ln 10$. Notably, the pH value was set to be zero in this work for simplicity; U was the applied potential.

3. Results and discussion

3.1. Structures, stabilities and properties of B-terminated surfaces

Since the crystal structures of cubic BP and BAs are identical except for the lattice constants, the atomic structures of their corresponding low-index surfaces, such as (100), (110), and (111), are also very similar. Thus, for simplicity, we chose BP as a representative when discussing the surface atomic structures, and Fig. 1 presents the atomic structures of the optimized (100), (110), and (111) surfaces of cubic BP, while the detailed data for BAs are given in Fig. S1 in the ESI.† Compared with the clean-cut surfaces, obvious surface reconstructions and relaxations occurred upon geometry optimization in order to reduce the surface energies or saturate the surface dangling bonds. In detail, for the BP (100) surface, two adjacent B atoms form B_2 dimers (bond length *ca.* 1.66 Å) to saturate the otherwise dangling bonds (Fig. 1a), while the bond between a surface B atom and its neighboring P atom is shortened to *ca.* 1.90 Å, which is slightly shorter than that (1.96 Å) in the bulk. In the case of the BP (110) surface (Fig. 1b), the surface B atoms take an obvious inward relaxation, leading to a shortened B–P bond of *ca.* 1.92 Å. On the BP (111) surface (Fig. 1c), the B and P atoms are located in slightly different planes: the B atoms are in the outermost layer, while the P atoms are in the inner layer, and the surface B–P bond length is *ca.* 1.89 Å due to the inward relaxation of surface B atoms. Note that almost the same surface reconstructions and/or relaxations can be observed for the (100), (110), and (111) surfaces of cubic BAs (Fig. S1†), and the surface relaxation behavior of cubic BP and BAs is very similar to that of cubic BN.[48–53]

In order to identify which surface is more dominantly exposed for both cubic BP and BAs, we calculated the surface energies of these three low-index crystal surfaces. Our results revealed that the B-terminated (100), (110), and (111) surfaces have similar surface energies in both BP and BAs, implying their similar thermodynamic stabilities and almost the same possibility to be exposed. In addition, we also explored the P or As-terminated (100) and (111) surfaces. We found that the P/As-terminated surfaces generally have higher surface energies than B-terminated ones, suggesting that the B-terminated surfaces have a higher thermodynamic stability and higher probability of natural exposure. Thus, we only focus on the NRR process on B-terminated surfaces in the following discussion.

Since electronic properties play an important role in the adsorption, activation, and subsequent reduction of N_2 on corresponding surfaces, we examined the local density of states (LDOS) of surface B atoms on the three considered low-index surfaces for both BP and BAs (Fig. 1 and S1†). The (111) surfaces are greatly spin-polarized with rather high spin magnetic moments (7.92 and 7.84 μ_B for BP and BAs, respectively), which are mainly contributed from the surface B atoms (Fig. S2†). Note that previous studies revealed that surface spin polarization facilitates the activation of N_2 molecules;[3,16,54] thus, the surface B atoms on the (111) surfaces may also have potential to activate inert N_2 molecules. In contrast, the (100) and (110) surfaces of BP and BAs have almost no spin polarization due to the formation a B–B dimer and the inward relaxation of surface B atoms, respectively. Note that the same polarization/non-polarization characteristics are observed in the corresponding surfaces in BN.[53,55] Interestingly, the LDOS of BP (111) (Fig. 1f) is obviously higher than those of the BP (100) and BP (110) surfaces (Fig. 1d and e) around the Fermi level. Similar results were also observed for cubic BAs (Fig. S1d–f†). Thus, the B atoms on the BP (111) and BAs (111) surfaces may accumulate more electrons around the Fermi level, which could be easily transferred into the antibonding orbitals of N_2, facilitating the activation of the inert N_2 molecule. Meanwhile, each B atom on the (111) surface forms three covalent bonds with neighboring P or As atoms, leaving one empty orbital to accept the lone pair electrons of N_2 molecules, which is very similar to the proposed "acceptance–donation" process observed in B-decorated g-C_3N_4 nanosheets.[28] All these analyses suggest that the (111) surfaces may possess higher chemical activity toward N_2 molecules than the (110) and (100) surfaces, which will be further discussed in the following sections.

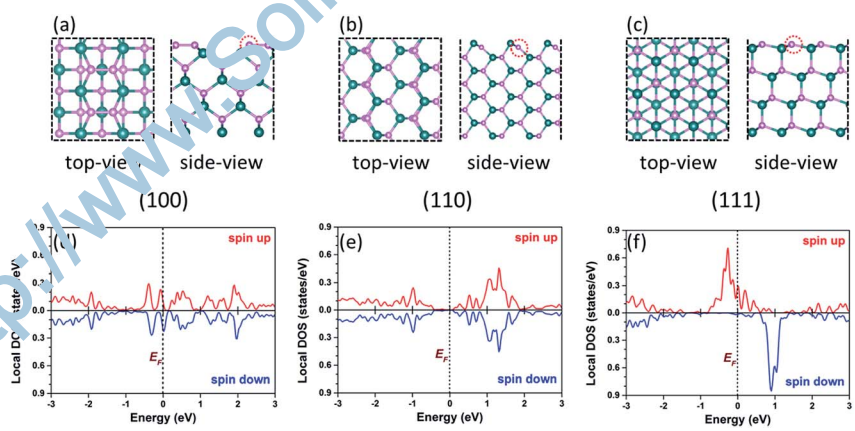

Fig. 1 Schematic atomic structures of (a) the (100) surface, (b) the (110) surface, and (c) the (111) surface of cubic BP. The local density of states (LDOSs) of surface B atoms marked with red dashed circles on (d) the (100) surface, (e) the (110) surface, and (f) the (111) surface of cubic BP. The Fermi level (E_F) was set to be zero and denoted by the black dashed line.

3.2. Adsorption of N_2 on B-terminated surfaces

The adsorption of N_2 on the catalyst surface is the first step in the NRR pathway, which is crucial for the subsequent reaction steps. Two different adsorption configurations, including end-on and side-on patterns, were considered for N_2 adsorption on all the relevant surfaces of BP (Fig. 2) and BAs (Fig. S3†). After full structural relaxation, the calculated N_2 adsorption energies are summarized in Table 1, while the corresponding free energies are given in Table S3.†

For simplicity, we took the (111) surface of BP as a representative to describe N_2 adsorption behavior. The adsorption energies of N_2 molecules on the BP (111) surface are −0.53 and −0.64 eV for the side-on and the end-on patterns, respectively. Thus, the end-on pattern is more favorable thermodynamically than the side-on one. Furthermore, the newly formed B–N bond lengths are *ca.* 1.47 Å (end-on) and 1.62 Å (side-on), respectively (Fig. 2c and d), which are shorter than that of BH_3NH_3 (1.65 Å), indicating strong adsorption of N_2 molecules on the (111) surface. Due to this strong adsorption, the B atoms adsorbed by N_2 extrude from the original plane by *ca.* 0.21 Å (side-on) and 0.16 Å (end-on), respectively.

Remarkably, the N≡N bond is elongated from 1.12 Å in a free N_2 molecule to 1.24 Å upon adsorption *via* the side-on manner. For comparison, for the end-on case, the N≡N bond of the adsorbed N_2 molecule is only slightly elongated to 1.13 Å. The difference in N_2 bond elongation can be well understood by the different amounts of charge transfer from the substrate to the N_2 molecule. According to Hirshfeld population analysis, charge transfer (0.16 electrons) in the side-on pattern is more significant than that (0.05 electrons) in the end-on case, which leads to the obvious elongation of the N–N bond in the side-on pattern. Note that similar bond elongation occurs for N_2 molecules on the BAs (111) surface (Fig. S3).

To get a deeper insight into the observed N_2 activation on the BP (111) surface, we further examined the charge density difference of N_2 adsorbed on the BP (111) (Fig. 3) and BAs (111) surfaces (Fig. S4†). Interestingly, the charge transfer is a "two-way" process, and N_2 adsorption follows the "acceptance–donation" process:[28] charge accumulation and depletion can be observed for both N_2 molecules and terminated B atoms, in which B atoms accept the lone-pair electrons and simultaneously donate electrons to the anti-bonding orbitals of N_2. Such an "acceptance–donation" process can be further confirmed by comparing the LDOS of the BP (111) and BAs (111) surfaces before and after N_2 adsorption (Fig. S5†), for both BP (111) and BAs (111) surfaces; the LDOS of surface B atoms clearly decreases and the spin polarization has been significantly quenched after N_2 adsorption with the side-on pattern (Fig. S2†). Overall, the above results reveal that an inert N_2 molecule can be sufficiently activated on the BP (111) and BAs (111) surfaces, which would facilitate its subsequent reduction reactions.

Table 1 The calculated adsorption energies (eV) of N_2 molecules with side-on and end-on patterns on the (100), (110) and (111) surfaces of BP and BAs

	BP			BAs		
Configuration	(100)	(110)	(111)	(100)	(110)	(111)
Side-on	−0.19	−0.12	−0.53	−0.07	−0.11	−0.56
End-on	−0.54	−0.44	−0.64	−0.55	−0.68	−0.76

In addition, we also explored N_2 adsorption behavior on the (100) and (110) surfaces. For these two surfaces, N_2 molecules prefer to be adsorbed *via* the end-on pattern (Fig. 2a and b) with adsorption energies ranging from −0.44 to −0.68 eV, while only weak adsorption is observed for the side-on pattern with adsorption energies ranging from −0.07 to −0.19 eV (Table 1). Thus, in the following sections, only the end-on pattern of N_2 molecules on the (100) and (110) surfaces was focused on for its further reduction.

3.3. Reaction mechanism and free energy for the NRR

The NRR process involves six net coupled proton and electron transfer steps, which can be simply written as: $N_2(g) + 6H^+ + 6e^- \rightarrow 2NH_3$. During the NRR process, an N_2 molecule is gradually hydrogenated by the protons from the solution and electrons from the electrode, producing various N_xH_y intermediates, including N_2H^*, $N_2H_2^*$, $N_2H_3^*$, $N_2H_4^*$, N^*, NH^*, NH_2^* and NH_3^*. As well understood, the N_2 molecule can be reduced to NH_3 through three reaction pathways, namely, enzymatic, distal, and alternating pathways.[9,23,28] In general, the side-on adsorbed N_2 can be reduced to NH_3 through an enzymatic mechanism, in which its two N atoms are hydrogenated alternately, and the second NH_3 will be generated immediately after the first one is released. For the end-on adsorption configuration, the NRR

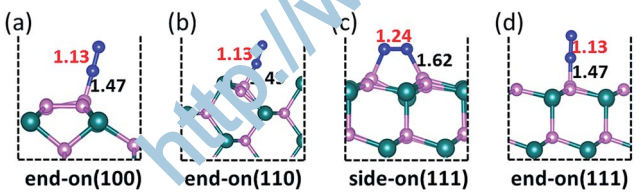

Fig. 2 Schematic diagram of all stable nitrogen adsorption configurations on (a) the (100) surface, (b) the (110) surface, (c) and (d) the (111) surface of BP, in which the value in red is the N–N bond length and the value in black is the B–N bond length (Å).

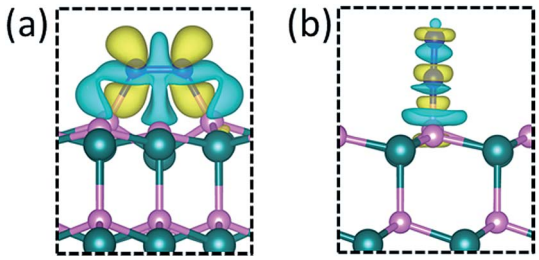

Fig. 3 Difference charge density of the BP (111) surface with the adsorption of N_2 *via* (a) side-on pattern and (b) end-on pattern, where the isosurface value is set to be 0.005 e $Å^{-3}$ and cyan and yellow regions represent positive and negative charges, respectively.

proceeds following either the distal or the alternating pathway. In the distal pathway, the remote N atom is firstly hydrogenated to release NH_3, while the two N atoms will be hydrogenated simultaneously in the alternating pathway. To evaluate the NRR catalytic activity, we computed the free energy changes (ΔG) of each elementary step in the NRR *via* the enzymatic, distal, and alternating mechanisms.

The computed Gibbs free energy diagrams of the NRR on the (111) surfaces of BP and BAs through the enzymatic pathway are presented in Fig. 4a and b, together with the corresponding adsorbed species structures. The free energy diagrams of distal and alternating pathways are listed in Fig. S6† (BP) and Fig. S7† (BAs) with the corresponding structures of the reaction intermediates. Notably, for the computation of free energies of each elementary step in the NRR, the involved vibrational frequencies, zero point energies, and entropic corrections of all intermediates are summarized in Table S4.†

Following the enzymatic pathway, on the BP (111) surface, the activated N_2 molecule with the side-on pattern will be firstly hydrogenated to N_2H^* species with a ΔG value of -0.44 eV. Subsequently, the formed N_2H^* species is further reduced to $NHNH^*$, $NHNH_2^*$, $NH_2^* + NH_2^*$, NH_2^* and NH_3^*. In this case, all the elementary steps are downhill in the free energy profiles, except for the formation of the second NH_3 ($NH_2^* + H^+ + e^- \rightarrow NH_3^*$) with a ΔG value of +0.12 eV (Fig. 4a). Thus, this step is the potential-determining step (PDS) for the whole NRR with a rather low limiting potential (-0.12 V). Remarkably, the direct desorption of NH_3 formed from the BP or BAs surface could be difficult due to its large free energy (1.20–1.60 eV). However, NH_3 desorption is not a problematic obstacle due to the following reasons: (1) the released energy (about 3.40 eV, Fig. 4) at the corresponding hydrogenation steps is large enough to overcome the required energy for the release of the formed NH_3 (1.20–1.60 eV);[28,29] (2) the formed NH_3^* can be

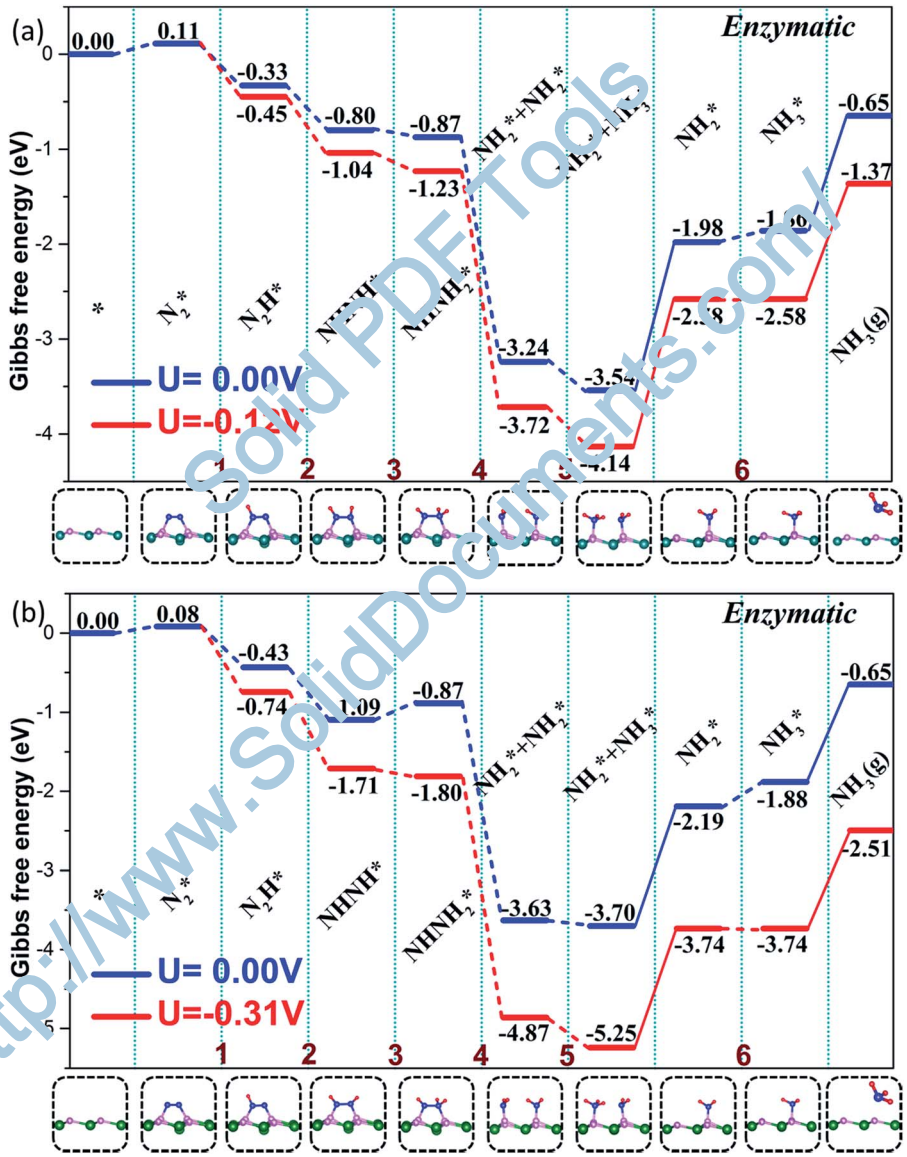

Fig. 4 Gibbs free energy diagrams for N_2 reduction through enzymatic mechanisms on (a) BP (111) surface and (b) BAs (111) surface at zero and applied potentials, together with the corresponding adsorbed species structures.

hydrogenated into NH_4^+ under strongly acidic conditions, which has been observed in previous reports on electrochemical reduction of nitric oxide.[56]

When the NRR proceeds through the distal or alternating pathways (Fig. S6†), the potential-determining step is located at the formation of the first NH_3 or the N_2H^* species due to the maximum ΔG value (0.99 or 0.49 eV), which is much higher than that of the enzymatic pathway (0.12 eV), suggesting that nitrogen reduction on the BP (111) surface prefers to take place through the enzymatic pathway. Similarly, on the BAs (111) surface, the enzymatic pathway is also the most favorable for the NRR (Fig. 4b), and the reaction step of $NH_2^* \rightarrow NH_3^*$ is the PDS with a free energy change of 0.31 eV, which is about two times higher than that of BP (0.12 eV).

Notably, though the side-on pattern is slightly less favorable than the end-on pattern for N_2 adsorption on the (111) surfaces, the free energies of the formed N_2H^* species in the side-on pattern in the enzymatic pathway are more stable by about 0.84 eV (BP) and 0.81 eV (BAs) than those in the end-on pattern. The activation barrier for N_2H^* to transfer from the end-on to side-on pattern is rather small (0.02 eV for BP and 0.01 eV for BAs) (for details, see Fig. S8 in the ESI†).

Thus, we also considered a mixed catalytic pathway, *i.e.*, N_2 is firstly adsorbed on the catalyst surface in the end-on pattern, followed by its hydrogenation to N_2H^* species with a side-on pattern, and the subsequent elementary steps follow the enzymatic pathway (Fig. S9 in ESI†). Note that in the actual reactions, this mixed pathway is the most favorable. Since the PDS is the formation of the second NH_3, the limiting potential in this preferred mixed catalytic pathway is the same as that in the enzymatic pathway (−0.12 V).

In addition, we explored the catalytic performance of the (100) and (110) surfaces of BP and BAs. Since only the end-on pattern is stable for N_2 adsorption on these surfaces, the NRR prefers to occur through the distal or the alternating pathway. We first studied the hydrogenation of the adsorbed N_2 molecule to N_2H^* species, and found that the free energy of N_2H^* formation on the (100) and (110) surfaces of BP or BAs is at least 0.66 eV, which is much larger than that of the corresponding (111) surfaces (0.12 eV for BP and 0.31 eV for BAs). Thus, the NRR activity of the (100)/(110) surfaces of BP and BAs is much lower than that of the corresponding (111) surfaces, and will not be further studied.

Our above studies revealed that the BP (111) surface exhibits the highest catalytic activity towards the NRR among all the considered surfaces and its limiting potential (−0.12 V) is even lower than that of recently reported B-decorated g-C_3N_4 with a record low limiting potential (−0.20 V).[28]

3.4. Stability against poisoning

The hydrogen evolution reaction (HER) is one of the competing electrochemical reactions against the NRR, since the adsorbed H could block the effective active sites and thus reduce the Faradaic efficiency. For the HER, due to the strong interaction between H and B atoms, the HER process is hindered by the Heyrovsky step ($H^* + H^+ + e^- \rightarrow H_2$) with computed free energy barriers of 1.38 and 1.52 eV, respectively (Fig. 5), which are much larger than that of the NRR (0.12 and 0.31 eV, Fig. 4) suggesting that the BP and BAs (111) surfaces exhibit outstanding catalytic performance for the NRR than the HER.

In addition, we also compared the difference in the adsorption strength between H* and N_2H^* species, because the formation of N_2H^* species is the first hydrogenation step and its adsorption strength on catalyst surfaces usually determines the overpotential requirement on catalysts. Thus, a promising NRR catalyst should be able to stabilize N_2H species.[57,58]

Note that electrochemical ammonia synthesis usually involves associative or dissociative pathways.[57,58] In both pathways, two hydrogenation mechanisms exist: (1) a Tafel-type mechanism,[59] in which the solvated protons from the solution first cover the catalyst surface and couple with electrons. Subsequently, the hydrogen adatoms react with N_2H_x or NH_x to yield NH_3. Notably, this mechanism is very slow at room temperature because the activation barriers for $H^* + NH_x^* \rightarrow NH_{x+1}^*$ reactions are generally larger than 1.00 eV. In particular, an applied bias can indirectly affect the thermochemical barrier by varying the concentrations of the reactants.[60,61] (2) A Heyrovsky-type mechanism,[62] in which the adsorbed N_2H_x or NH_x species will be hydrogenated by direct attachment of protons from the solution and electrons from the electrode, and the applied bias has a direct influence on the energy barrier. In this study, the Heyrovsky-type mechanism was considered for the synthesis of ammonia from the NRR at room temperature, and the same assumptions have been widely employed in the electrochemical reaction of CO_2 and O_2.[63,64] The computed adsorption energies of N_2H^* in the side-on pattern are −3.38 eV (BP) and −3.49 eV (BAs), respectively, much more negative than that of H* (−1.69 and −1.83 eV, respectively). Therefore, the N_2H^* species is energetically favored to be adsorbed on the electrocatalysts rather than the H species, and hydrogen poisoning is not a big concern).

Clearly, the (111) surfaces of BP and BAs possess an extremely excellent catalytic activity and selectivity for the NRR. However, are these two surfaces stable under ambient conditions? To address this question, we performed AIMD

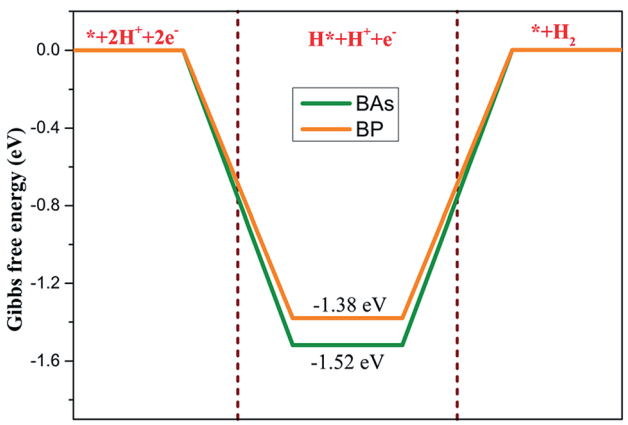

Fig. 5 Gibbs free energy diagrams of the HER on the BP and BAs (111) surfaces.

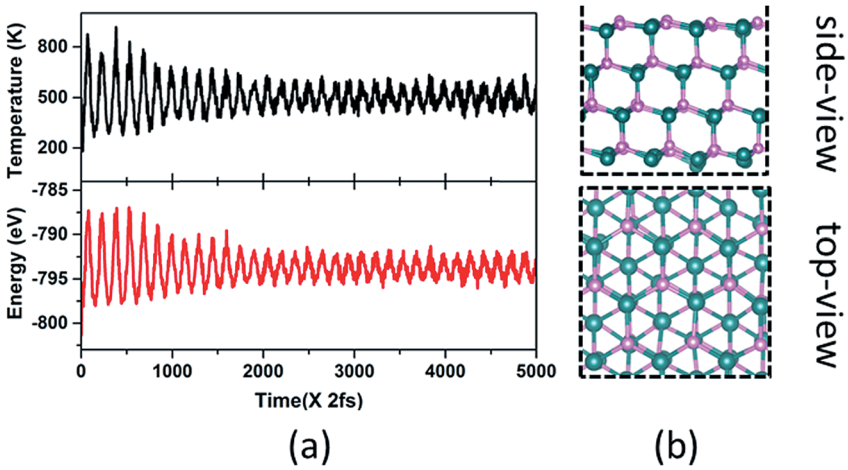

Fig. 6 (a) Variations of temperature and energy against the time for AIMD simulations of BP; the simulation is run at 500 K for 10 ps with a time step of 2 fs. (b) Schematic diagram of the structure after dynamics simulation.

simulations at 500 K for 10 ps with a time step of 2 fs. Taking the BP (111) surface as an example (Fig. 6), the temperature and energy oscillate near the equilibrium state. The atomic structure of the BP (111) surface remains intact without any obvious structural distortion during the AIMD simulation period, indicating the high stability of BP (111) surfaces. Such a high stability is also observed for the BAs (111) surface (Fig. S10). With high stability at 500 K as demonstrated by AIMD simulations, we believe that the (111) surfaces of BP and BAs can be utilized as a highly efficient NRR electrocatalyst under ambient conditions (300 K).

Since the NRR generally proceeds in an aqueous solution, the proposed B-terminated (111) surfaces in our work could interact with environmental water. Thus, we also considered the adsorption of H_2O molecules on the BP and BAs (111) surfaces to evaluate their stability in practical applications. Our results demonstrated that H_2O could be adsorbed on the surfaces of the two catalysts with an adsorption energy of −0.95 eV, which is slightly more negative than that of the N_2 molecule (about −0.76 eV), indicating that the B-terminated catalysts prefer to be covered with H_2O. However, the adsorbed H_2O will easily react with free N_2 molecules with the help of protons and electrons to form N_2H species (*i.e.*, $H_2O^* + N_2 + H^+ + e^- \rightarrow N_2H^* + H_2O$) with a free energy of −0.06 eV on BP (111) and −0.16 eV on BAs (111) surfaces, as N_2H^* species exhibits a much stronger adsorption strength (about −3.40 eV) on the two catalysts than H_2O (−0.95 eV). Thus, the catalytic performance of the two B-terminated catalysts can be well preserved in an aqueous solution, which has been observed in a recent experimental study.[65] Remarkably, the ionic liquids that have high N_2 solubility was recently adopted to replace water as the electrolyte to achieve a high conversion efficiency for N_2 electroreduction to ammonia under ambient conditions, which could suppress the unwanted HER and H_2O poisoning effects.[66]

Finally, we investigated the interaction between our newly proposed catalysts with O_2. Similar to the well-known black phosphorene[67,68] and silicene,[69] the two proposed B-terminated surfaces also exhibit high chemical reactivity towards O_2 molecules, leading to the formation of oxide units. Thus, chemisorption-induced oxidation will be a major cause for the degradation of BP and BAs catalysts. A promising solution to avoid problematic oxidation is to develop passivation and encapsulation by an inert material, in the same way as we used BN,[70] polymethyl methacrylate (PMMA),[71] and alumina or AlO_x,[72,73] to protect the otherwise unstable phosphorene and silicene. Among these encapsulation techniques, AlO_x encapsulation using atomic layer deposition is probably the most appealing in terms of industrial application and scalability, which can make the encapsulated phosphorene stable for more than 2 weeks and withstand more than 5000 bending cycles.[72,73] On the other hand, the whole NRR process could be performed under oxygen-free conditions, as Wang and coworkers recently demonstrated in their experiments using black phosphorus nanosheets to selectively catalyze the NRR under ambient conditions.[74] Overall, though BP and BAs could be unstable in air, we strongly believe that their superior NRR catalytic performance can be achieved in the quite near future by encapsulation techniques or under oxygen-free conditions. We also hope that our theoretical studies could inspire experimental studies to explore the potentials of B-terminated surfaces for the NRR and other important reactions.

4. Conclusions

In this work, we explored the NRR properties of the (100), (110), and (111) surfaces of cubic BP and BAs using DFT calculations. Our computations revealed that the (111) surfaces have comparable surface energies with those of the (100) and (110) surfaces, and are stable under ambient conditions. Among all the considered surfaces, the (111) surfaces of BP and BAs exhibit superior catalytic performance for the NRR due to their rather low limiting potential (−0.12 and −0.31 V for BP and BAs, respectively) and strong ability to inhibit hydrogen evolution reactions. Therefore, cubic BP and BAs with mainly exposed

(111) surfaces are a new class of metal-free low-cost electrocatalysts with a large active region for N_2 reduction, and can be utilized as highly efficient electrocatalysts for sustainable NH_3 production.

Conflicts of interest

There are no conflicts to declare.

Acknowledgements

This work was financially supported in China by the National Natural Science Fund of China (No. 51472249), the Natural Science Funds for Distinguished Young Scholar of Heilongjiang Province (No. JC2018004), and the Excellent Young Foundation of Harbin Normal University (Grant No. XKYQ201304), and in the USA by the NSF-CREST Center for Innovation, Research and Education in Environmental Nanotechnology (CIRE2N) (Grant Number HRD-1736093). Most computations were performed on TianHe-1(A) at the National Supercomputer Center in Tianjin, and a portion of this research used computational resources at the Center for Nanophase Materials Sciences, which is a DOE Office of Science User Facility.

References

1 H. Hirakawa, M. Hashimoto, Y. Shiraishi and T. Hirai, *J. Am. Chem. Soc.*, 2017, **139**, 10929–10936.
2 H. Li, J. Shang, Z. Ai and L. Zhang, *J. Am. Chem. Soc.*, 2015, **137**, 6393–6399.
3 X.-F. Li, Q.-K. Li, J. Cheng, L. Liu, Q. Yan, Y. Wu, X. H. Zhang, Z.-Y. Wang, Q. Qiu and Y. Luo, *J. Am. Chem. Soc.*, 2016, **138**, 8706–8709.
4 S. Licht, B. Cui, B. Wang, F.-F. Li, J. Lau and S. Liu, *Science*, 2014, **345**, 637–640.
5 M. Kitano, Y. Inoue, Y. Yamazaki, F. Hayashi, S. Kanbara, S. Matsuishi, T. Yokoyama, S.-W. Kim, M. Hara and H. Hosono, *Nat. Chem.*, 2012, **4**, 934.
6 M. A. van Kessel, D. R. Speth, M. Albertsen, P. H. Nielsen, H. J. O. den Camp, B. Kartal, M. S. Jetten and S. Lücker, *Nature*, 2015, **528**, 555.
7 S. J. Li, D. Bao, M. M. Shi, B. R. Wulan, J. M. Yan and Q. Jiang, *Adv. Mater.*, 2017, **29**, 1700001.
8 M. Kitano, S. Kanbara, Y. Inoue, N. Kuganathan, P. V. Sushko, T. Yokoyama, M. Hara and H. Hosono, *Nat. Commun.*, 2015, **6**, 6731.
9 X. Cui, C. Tang and Q. Zhang, *Adv. Energy Mater.*, 2018, **8**, 1800369.
10 T. Spatzal, M. Aksoyoglu, L. Zhang, S. L. Andrade, E. Schleicher, S. Weber, D. C. Rees and O. Einsle, *Science*, 2011, **334**, 940.
11 L. M. Azofra, C. Li, D. R. MacFarlane and C. Sun, *Energy Environ. Sci.*, 2016, **9**, 2545–2549.
12 L. Zhang, Z. J. Zhao and J. Gong, *Angew. Chem., Int. Ed.*, 2017, **56**, 11326–11353.
13 M. Li, H. Huang, J. Low, C. Gao, R. Long and Y. Xiong, *Small Methods*, 2018, **2**, 1800388.
14 Y. Liu, Y. Su, X. Quan, X. Fan, S. Chen, H. Yu, H. Zhao, Y. Zhang and J. Zhao, *ACS Catal.*, 2018, **8**, 1186–1191.
15 Q. Qin, T. Heil, M. Antonietti and M. Oschatz, *Small Methods*, 2018, **2**, 1800202.
16 Z. Wei, Y. Zhang, S. Wang, C. Wang and J. Ma, *J. Mater. Chem. A*, 2018, **6**, 13790–13796.
17 X. Wang, W. Wang, M. Qiao, G. Wu, W. Chen, T. Yuan, Q. Xu, M. Chen, Y. Zhang, X. Wang, J. Wang, J. Ge, X. Hong, Y. Li, Y. Wu and Y. Li, *Sci. Bull.*, 2018, **63**, 1246–1253.
18 M. Nazemi, S. R. Panikkanvalappil and M. A. El-Sayed, *Nano Energy*, 2018, **49**, 316–323.
19 S. Hu, X. Qu, J. Bai, P. Li, Q. Li, F. Wang and L. Song, *ACS Sustainable Chem. Eng.*, 2017, **5**, 6863–6872.
20 Á. B. Höskuldsson, Y. Abghoui, A. B. Gunnarsdóttir and E. Skúlason, *ACS Sustainable Chem. Eng.*, 2017, **5**, 10327–10333.
21 H. Liu, L. Wei, F. Liu, Z. Pei, J. Shi, Z.-j. Wang, D. He and Y. Chen, *ACS Catal.*, 2019, **9**, 5245–5267.
22 J. Wang, L. Yu, L. Hu, G. Chen, H. Xin and X. Feng, *Nat. Commun.*, 2018, **9**, 1795.
23 Z. Chen, J. Zhao, C. R. Cabrera and Z. Chen, *Small Methods*, 2018, **2**, 1800368.
24 K. Ithisuphalap, H. Zhang, L. Guo, Q. Yang, H. Yang and G. Wu, *Small Methods*, 2018, **2**, 1800352.
25 M.-A. Légaré, G. Bélanger-Chabot, R. D. Dewhurst, E. Welz, I. Krummenacher, B. Engels and H. Braunschweig, *Science*, 2018, **359**, 896–900.
26 D. L. Broere and P. L. Holland, *Science*, 2018, **359**, 871.
27 X. Yu, P. Han, Z. Wei, L. Huang, Z. Gu, S. Peng, J. Ma and G. Zheng, *Joule*, 2018, **2**, 1610–1622.
28 C. Ling, X. Niu, Q. Li, A. Du and J. Wang, *J. Am. Chem. Soc.*, 2018, **140**, 14161–14168.
29 W. Qiu, X.-Y. Xie, J. Qiu, W.-H. Fang, R. Liang, X. Ren, X. Ji, G. Cui, A. M. Asiri and G. Cui, *Nat. Commun.*, 2018, **9**, 3485.
30 X. Zheng, S. Li, C. Li, Y. Lv, X. Liu, P. Y. Huang, D. A. Broido, E. Lv and D. G. Cahill, *Adv. Funct. Mater.*, 2018, **28**, 1805116.
31 L. Shi, P. Li, W. Zhou, T. Wang, K. Chang, H. Zhang, T. Kako, G. Liu and J. Ye, *Nano Energy*, 2016, **28**, 158–163.
32 J. S. Kang, M. Li, H. Wu, H. Nguyen and Y. Hu, *Science*, 2018, **361**, 575–578.
33 S. Chae, K. Mengle, J. T. Heron and E. Kioupakis, *Appl. Phys. Lett.*, 2018, **113**, 212101.
34 T.-H. Liu, B. Song, L. Meroueh, Z. Ding, Q. Song, J. Zhou, M. Li and G. Chen, *Phys. Rev. B*, 2018, **98**, 081203.
35 N. Izyumskaya, D. O. Demchenko, S. Das, Ü. Özgür, V. Avrutin and H. Morkoç, *Adv. Electron. Mater.*, 2017, **3**, 1600485.
36 G. Kresse, *Phys. Rev. B: Condens. Matter Mater. Phys.*, 1996, **54**, 11169.
37 J. P. Perdew, J. A. Chevary, S. H. Vosko, K. A. Jackson, M. R. Pederson, D. J. Singh and C. Fiolhais, *Phys. Rev. B: Condens. Matter Mater. Phys.*, 1992, **46**, 6671.
38 P. E. Blöchl, *Phys. Rev. B: Condens. Matter Mater. Phys.*, 1994, **50**, 17953.
39 J. P. Perdew and Y. Wang, *Phys. Rev. B: Condens. Matter Mater. Phys.*, 1992, **45**, 13244.

40 J. Neugebauer and M. Scheffler, *Phys. Rev. B: Condens. Matter Mater. Phys.*, 1992, **46**, 16067.
41 S. Grimme, *J. Comput. Chem.*, 2006, **27**, 1787–1799.
42 G. Henkelman, B. P. Uberuaga and H. Jónsson, *J. Chem. Phys.*, 2000, **113**, 9901–9904.
43 F. L. Hirshfeld, *Theor. Chim. Acta*, 1977, **44**, 129–138.
44 B. Delley, *J. Chem. Phys.*, 1990, **92**, 508–517.
45 S. Nosé, *J. Chem. Phys.*, 1984, **81**, 511–519.
46 G. Bussi, D. Donadio and M. Parrinello, *J. Chem. Phys.*, 2007, **126**, 014101.
47 J. K. Nørskov, J. Rossmeisl, A. Logadottir, L. Lindqvist, J. R. Kitchin, T. Bligaard and H. Jonsson, *J. Phys. Chem. B*, 2004, **108**, 17886–17892.
48 K. Kádas, G. Kern and J. Hafner, *Surf. Sci.*, 2000, **454**, 494–497.
49 N. Ooi and J. B. Adams, *Surf. Sci.*, 2005, **574**, 269–286.
50 M.-F. Ng, M. K. Teo, K. H. Lim, L. Zhou, M. B. Sullivan and S.-W. Yang, *Diamond Relat. Mater.*, 2008, **17**, 2048–2053.
51 J. Yamauchi, M. Tsukada, S. Watanabe and O. Sugino, *Phys. Rev. B: Condens. Matter Mater. Phys.*, 1996, **54**, 5586.
52 M.-H. Tsai and C. Liu, *Phys. Rev. B: Condens. Matter Mater. Phys.*, 2001, **63**, 073305.
53 G. Cappellini, G. Satta, M. Palummo and G. Onida, *Phys. Rev. B: Condens. Matter Mater. Phys.*, 2002, **66**, 115412.
54 X. Guo and S. Huang, *Electrochim. Acta*, 2018, **284**, 392–399.
55 K. Kadas, G. Kern and J. Hafner, *Phys. Rev. B: Condens. Matter Mater. Phys.*, 1998, **58**, 15636.
56 H.-J. Chun, V. Apaja, A. Clayborne, K. Honkala and J. Greeley, *ACS Catal.*, 2017, **7**, 3869–3882.
57 J.-H. Montoya, C. Tsai, A. Vojvodic and J. K. Nørskov, *ChemSusChem*, 2015, **8**, 2180–2186.
58 E. Skulason, T. Bligaard, S. Gudmundsdóttir, F. Studt, J. Rossmeisl, F. Abild-Pedersen, T. Vegge, H. Jonsson and J. K. Nørskov, *Phys. Chem. Chem. Phys.*, 2012, **14**, 1235–1245.
59 J. Tafel, *Z. Phys. Chem., Stoechiom. Verwandtschaftsl.*, 1905, **50**, 641.
60 K. Honkala, A. Hellman, I. N. Remediakis, A. Logadottir, A. Carlsson, S. Dahl, C. H. Christensen and J. K. Nørskov, *Science*, 2005, **307**, 555–558.
61 S. Wang, V. Petzold, V. Tripkovic, J. Kleis, J. G. Howalt, E. Skúlason, E. M. Fernandez, B. Hvolbaek, G. Jones, A. Toftelund, H. Falsig, M. Björketun, F. Studt, F. AbildPedersen, J. Rossmeisl, J. K. Nørskov and T. Bligaard, *Phys. Chem. Chem. Phys.*, 2011, **13**, 20760–20765.
62 J. Heyrovsky, *Recl. Trav. Chim. Pays-Bas*, 1927, **46**, 582.
63 A. A. Peterson, F. Abild-Pedersen, F. Studt, J. Rossmeisl and J. K. Nørskov, *Energy Environ. Sci.*, 2010, **3**, 1311–1315.
64 J. Rossmeisl, Z.-W. Qu, H. Zhu, G.-J. Kroes and J. K. Nørskov, *J. Electroanal. Chem.*, 2007, **607**, 83–89.
65 M. Wang, S. Liu, T. Qian, J. Liu, J. Zhou, H. Ji, J. Xiong, J. Zhong and C. Yan, *Nat. Commun.*, 2019, **10**, 341.
66 F. Zhou, L. M. Azofra, M. Ali, M. Kar, A. N. Simonov, C. McDonnell-Worth, C. Sun, X. Zhang and D.-R. MacFarlane, *Energy Environ. Sci.*, 2017, **10**, 2516–2520.
67 L. Kou, C. Chen and S. C. Smith, *J. Phys. Chem. Lett.*, 2015, **6**, 2794–2805.
68 A. Carvalho, M. Wang, X. Zhu, A. S. Rodin, H. Su and A. H. C. Neto, *Nat. Rev. Mater.*, 2016, **1**, 16061.
69 L. Tao, E. Cinquanta, D. Chiappe, C. Grazianetti, M. Fanciulli, M. Dubey, A. Molle and D. Akinwande, *Nat. Nanotechnol.*, 2015, **10**, 227.
70 R. A. Doganov, S. P. Koenig, Y. Yeo, K. Watanabe, T. Taniguchi and B. Özyilmaz, *Appl. Phys. Lett.*, 2015, **106**, 083505.
71 V. Tayari, N. Hemsworth, I. Fakih, A. Favron, E. Gaufrès, G. Gervais, R. Martel and T. Szkopek, *Nat. Commun.*, 2015, **6**, 7702.
72 J. Na, Y. T. Lee, J. A. Lim, D. K. Hwang, G.-T. Kim, W. K. Choi and Y. W. Song, *ACS Nano*, 2014, **8**, 11753–11762.
73 J. S. Kim, Y. Liu, W. Zhu, S. Kim, D. Wu, L. Tao, A. Dodabalapur, K. Lai and D. Akinwande, *Sci. Rep.*, 2015, **5**, 8989.
74 L. Zhang, L. Ding, X. Yang and H. Wang, *Angew. Chem., Int. Ed.*, 2019, **131**, 2638–2642.

